ACS MATERIALS LETTERS

www.acsmaterialsletters.org

Quantification of the Helical Morphology of Chiral Gold Nanorods

Wouter Heyvaert, Adrián Pedrazo-Tardajos, Ajinkya Kadu, Nathalie Claes, Guillermo González-Rubio, Luis M. Liz-Marzán, Wiebke Albrecht,* and Sara Bals*

Cite This: *ACS Materials Lett.* 2022, 4, 642−649

Read Online

ACCESS | Metrics & More | Article Recommendations | Supporting Information

ABSTRACT: Chirality in inorganic nanoparticles and nanostructures has gained increasing scientific interest, because of the possibility to tune their ability to interact differently with left- and right-handed circularly polarized light. In some cases, the optical activity is hypothesized to originate from a chiral morphology of the nanomaterial. However, quantifying the degree of chirality in objects with sizes of tens of nanometers is far from straightforward. Electron tomography offers the possibility to faithfully retrieve the three-dimensional morphology of nanomaterials, but only a qualitative interpretation of the morphology of chiral nanoparticles has been possible so far. We introduce herein a methodology that enables us to quantify the helicity of complex chiral nanomaterials, based on the geometrical properties of a helix. We demonstrate that an analysis at the single particle level can provide significant insights into the origin of chiroptical properties.

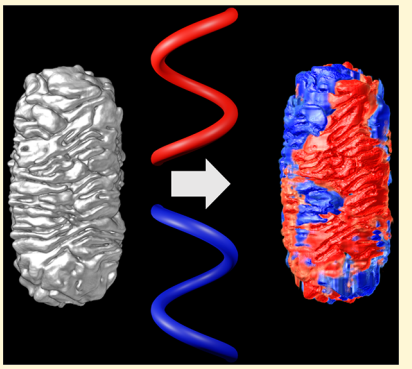

Chiral features in metal nanoparticles (NP) result in chiroptical properties, of interest to many applications, such as enantioselective catalysis or separation, chiral sensing, drug delivery, and the generation of circularly polarized light (CPL).[1−8] These applications arise from the different interactions of chiral plasmonic NPs with left- and right-handed CPL. Therefore, much effort has been put into the development of NPs with complex structures and morphologies.[9−17] The properties of such nanomaterials are usually characterized by measuring their circular dichroism (CD), which quantifies the interaction of an ensemble of particles with CPL.[18] Under certain conditions, such measurements can also be performed for single nanoparticles, which may help account for heterogeneity in morphology and optical response.[19−21] Multiple factors can be at the origin of the recorded CD signal, such as a chiral morphology, chiral features in the crystalline structure, or the presence of chiral molecules at or near the surface of the chiral NPs.[1,7,22−25] To obtain NPs with tailored chiroptical properties, it is thus important to understand the connection between the CD signal and the NP morphology.

Electron microscopy is a suitable technique to investigate the structure of single chiral NPs. However, neither scanning electron microscopy (SEM) nor (scanning) transmission electron microscopy ((S)TEM) can faithfully reveal the complete 3D structure of the NPs.[14,26,27] An excellent alternative is electron tomography (ET), a technique that allows for the reconstruction of the 3D structure of nanomaterials from a tilt series of 2D STEM projection images. ET has been applied to visualize the 3D structure of chiral Au NPs in great detail.[10,28,29] For relatively simple structures, one can manually measure characteristics such as the helical pitch. Unfortunately, more complex structures, such as the chiral Au nanorods (NR) that we introduced in previous work, are more difficult to quantify on the basis of a purely visual inspection.[10] We therefore used 3D Fourier transformation (FT) of high-quality 3D ET reconstructions to identify chiral features on the NRs. However, this approach could not provide a quantitative measure of the NP chirality, or even clearly resolve their handedness.[10]

The Hausdorff chirality measure has previously been used to quantify chirality.[30] This method is based on minimizing the "Hausdorff distance" between the molecule and its mirror image, where a molecule is represented by a set of points in 3D space and each point represents a single atom. The chirality measure is defined as the ratio between the minimum Hausdorff distance and the diameter of the set of points. Since the number of points required to accurately represent a NP quickly rises for complex shapes, optimization becomes exceedingly demanding in terms of computation time.

Received: January 20, 2022
Accepted: March 2, 2022
Published: March 8, 2022

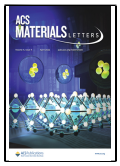

https://doi.org/10.1021/acsmaterialslett.2c00055
ACS Materials Lett. 2022, 4, 642−649

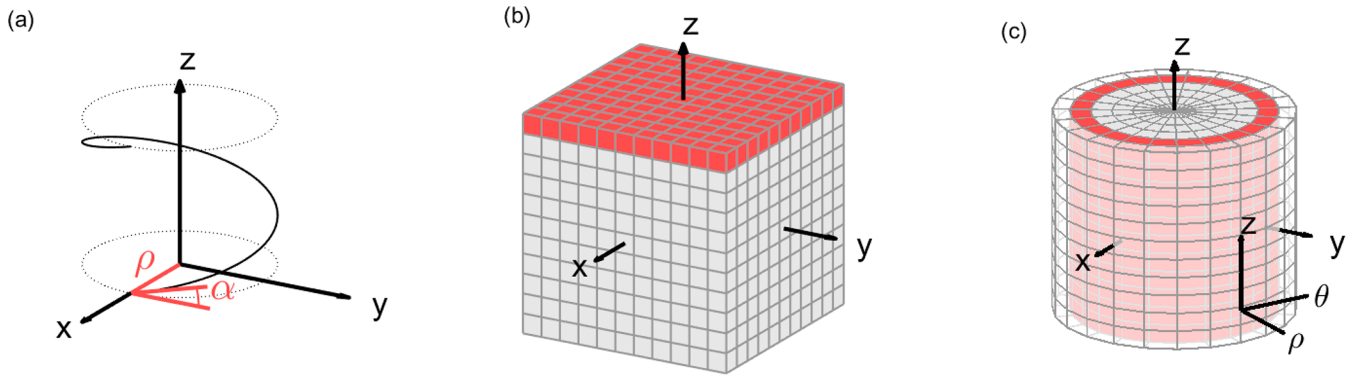

Figure 1. Illustration of the base geometries used in the proposed method: (a) a helix around the *z*-axis with radius ρ and inclination angle α; (b) a discrete voxel grid in Cartesian coordinates, where each cube is a voxel; and (c) a discrete voxel grid in cylindrical coordinates, where the voxels are no longer cubes, but trapezoidal prisms. An orthoslice at constant *z* and a cylindrical section at constant ρ are highlighted in red in b and c, respectively.

Moreover, the Hausdorff chirality measure can quantify the degree of chirality of a given system but is unable to distinguish between left- and right-handed chirality. Other methods have also been proposed to identify mirror symmetry, but they are all specifically designed for molecular structures and/or face the same problem of computational requirements and inability to detect handedness.[22,31−34] Alternatively, the chirality of elongated nanocrystals was analyzed by dividing the crystal into thin layers.[35] The orientation of each layer was determined using principal component analysis and the difference in orientation between subsequent layers was used as a measure of chirality. This is a viable approach, but it requires that the orientation of the layers in the object can be determined, which is not always possible. Therefore, we are still missing a reliable method that can objectively quantify morphological chirality in single NPs, based on ET. Such a method would be extremely useful to gain the necessary insights on structural enhancements that can eventually be used to improve the chiroptical activity of NPs.

We present herein a method to quantitatively investigate the helicity of single NPs, based on ET reconstructions. The methodology is used to identify helical features in the NP morphology and to extract parameters such as the inclination angle of such features. This approach will thus enable a quantitative investigation of the connection between NP shape and features in the corresponding CD spectrum, eventually leading to the optimization of chiral NPs.

METHODOLOGY

An object is chiral when its mirror image cannot be translated or rotated to completely overlap with the original shape.[36] Helicity, on the other hand, is more vaguely defined as the extent to which a structure resembles or contains helices or helix-like features. Helical shapes are always chiral but additionally present features that are easier to interpret, such as a well-defined handedness and helical pitch or inclination angle. Since most synthesis efforts toward chiral nanoparticles make use of helical growth, we designed a method to quantify helicity rather than chirality, even though chirality is the more general characteristic. Our method is specifically designed for the analysis of chiral NRs, which present attractive properties.[10,14,25,29] In a pioneering example, González-Rubio et al. were able to synthesize Au NRs with tunable chiroptical properties.[10] Beyond the initial qualitative interpretation of ET reconstructions for such particles, our method can extract quantitative information on chirality. Although our methodology has been designed for NRs, only a few assumptions on the input data were made. The method is thus relevant to most types of helical (nano)structures, as exemplified below.

The basis of our method is strongly connected to the properties of a helix, corresponding to (i) a central axis, (ii) the distance ρ between the helix and its central axis, and (iii) the angle of inclination α (Figure 1a). A helical shape can be described as a superposition of (parts of) individual helices, such that quantifying the helicity of an object can be simplified into detecting a sum of helices. We furthermore assume that the central axis is the same for all helices within a given shape and that it can be identified manually. The central axis for NRs will be parallel to its longitudinal symmetry axis and will pass through its center of mass.

As a first step, the ET reconstruction of the object of interest is oriented such that the central axis becomes the *z* axis of the defined coordinate system. Our method then searches for the presence of helices, for each combination of ρ and α. In a cylindrical coordinate system, helices around the *z* axis correspond to straight lines. Since an ET reconstruction is represented on a discrete voxel grid in Cartesian coordinates, as illustrated in Figure 1b, it should therefore be converted into a discrete voxel grid in cylindrical coordinates by linear interpolation (Figure 1c). This allows us to separately investigate concentric cylindrical 2D sections at constant ρ, such as the red section in Figure 1c.

To illustrate the different steps of our method, we created a 3D model of a rod with a right-handed helical shell, shown in Figure 2a. The model consists of an achiral cylindrical core with radius ρ_{core} = 64 voxels and height h = 256 voxels. Wrapped around this core is a chiral shell comprising two helices (blue and red in Figure 2a), each wrapping the core 2.5 times and extending to a radius ρ_{shell} = 96 voxels.

Two different cylindrical sections through the model are shown in Figure 2b,c. The presence of helices in our model translates into diagonal lines in the cylindrical sections. For each cylindrical section (at different radii ρ), we can then compute the so-called directionality, to identify the preferred orientation of the diagonal lines. The directionality can be extracted from the gradient of the cylindrical section, which gives the direction of greatest change in intensity and the rate of change in intensity in each pixel of the cylindrical section.[37] The direction of the gradient is therefore orthogonal to the orientation of diagonal features in the cylindrical sections. The

https://doi.org/10.1021/acsmaterialslett.2c00055
ACS Materials Lett. 2022, 4, 642−649

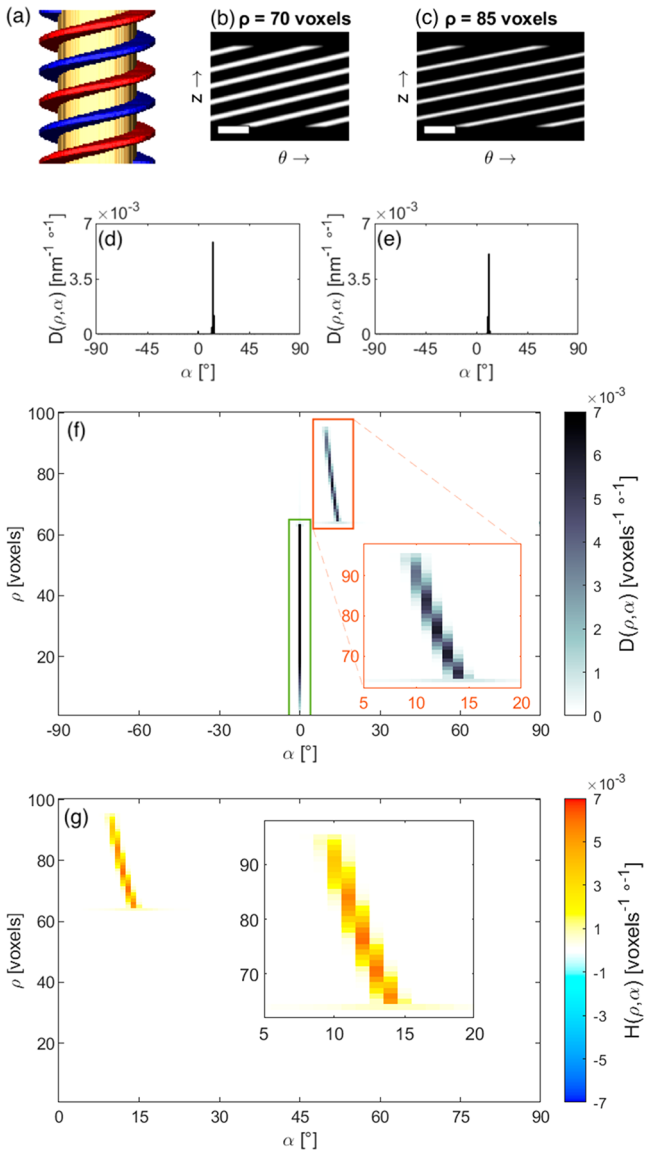

Figure 2. A simulated helix (a) with two of its cylindrical sections at ρ = 70 voxels (b) and ρ = 85 voxels (c). The scale bars are 100 voxels wide. The model consists of an achiral core (yellow) enveloped by two helices (blue and red). The directionality for the two cylindrical sections is shown in d and e, respectively, and the directionality of all cylindrical sections is combined in a histogram (f), to obtain the directionality of the 3D helix in cylindrical coordinates. Two main features in f are marked by green and orange boxes, and the orange region is enlarged in the inset. (g) Helicity function $H(\rho,\alpha)$ histogram and zoomed view (inset) of the peak corresponding to the helical shell of the model. Note that the line is not vertical due to the different angles involved in the model helix.

relative presence, or strength, of diagonal features in one cylindrical section can be quantified from the magnitude of the gradient. As such, one can create a histogram with inclination angles on the horizontal axis and the relative presence of features with each inclination angle on the vertical axis. Such a histogram can be filled by adding the magnitude of the gradient in each pixel to the histogram bin corresponding to the inclination angle in that pixel, as shown in Figure 2d and e for the two selected cylindrical sections. This process is visualized in more detail in Figure S1. The process is repeated for every cylindrical section, and the results are recombined into a 2D histogram to extract the directionality D (ρ,α) of the 3D shape, expressed in units of $[D] = [\rho]^{-1}[\alpha]^{-1}$ (Figure 2f). The directionality is normalized such that the sum over the complete 2D histogram equals 1 (see section 1 in the SI for more details).

The result for our model shows two strong peaks, highlighted by a green and an orange rectangle in Figure 2f. A vertical peak is present at $\alpha = 0°$ (green), which stems from the top and bottom edges of the particle. Another peak, ranging from $\alpha = 14°$ at $\rho = 64$ voxels to $\alpha = 10°$ at $\rho = 96$ voxels (orange), corresponds to the helical shell in the model. The inclination angle for the directionality is defined in the range $[-90°, 90°]$. A helix is thus left-handed for $\alpha \in]-90°, 0°[$, right-handed if $\alpha \in]0°, 90°[$, and not helical when α equals 0° or 90°, corresponding to horizontal or vertical features, respectively. The peak marked in green is not helical, whereas the peak marked in orange is only present at positive inclination angles. We therefore conclude that the shell is right-handed helical. It should be noted that the orange peak is slightly curved, indicating different inclination angles α at different radii ρ. Indeed, in the simulated helical rod, the helices wrap around the core with a period of 102 voxels in the z direction. Consequently, different inclination angles are required at different radii, as visible in Figure 2a.

On the basis of a visual inspection of more complex shapes such as those investigated in ref 10, it becomes more challenging to interpret directionality plots, which are expected to contain different contributions at both positive and negative inclination angles.[10] To enable an objective interpretation, we define a helicity function $H(\rho,\alpha)$, as the difference between right- and left-handed bins in the directionality $D(\rho,\alpha)$:

$$H(\rho, \alpha) = D(\rho, \alpha) - D(\rho, -\alpha)$$

for $\alpha \in [0°, 90°]$. Consequently, the helicity function will be positive if there are more right-handed features, or negative if left-handed features are more abundant. In the case where the numbers of left- and right-handed features are equal, the helicity function will become zero. The helicity function histogram for our model is shown in Figure 2g. A strong positive (right-handed) signal is present at the same inclination angles as those for the peak marked by an orange box in Figure 2f. Since $\alpha = 0°$ corresponds to nonhelical features, the peak marked by a green box is not present in the helicity function, i.e., $D(\rho,0°) = D(\rho,-0°)$.

A single parameter that indicates the total helicity of a given NP can be useful to compare the degree of helicity for different NPs. Such a measure can be obtained by calculating the integral of the helicity function, which reduces to a sum if the helicity function is discrete:

$$H_{\text{total}} = \sum_{\rho} \sum_{\alpha} H(\rho, \alpha) \Delta\rho \Delta\alpha$$

with $H_{\text{total}} \in [-1,1]$ due to the normalization of the directionality (see SI for more details). Positive values indicate right-handed helicity, negative values indicate left-handed helicity, and values close to zero indicate no overall helicity (even though certain parts of a NP may show helicity, which may be compensated by other areas within the same NP). More details on the calculation of $H(\rho,\alpha)$ and H_{total} are presented in section 2 of the SI, where the computational efficiency of the method is also discussed (Figure S2).

https://doi.org/10.1021/acsmaterialslett.2c00055
ACS Materials Lett. 2022, 4, 642−649

Table 1. Experimental Details of Five Selected NRs Used to Test the Method[a]

particle	micelle	seed diameter [nm]	seed height [nm]	diameter [nm]	height [nm]	expected handedness
R1	(*R*)-BINAMINE	46	139	127	216	right-handed
R2	(*R*)-BINAMINE	48	143	131	223	right-handed
S1	(*S*)-BINAMINE	46	131	135	212	left-handed
S2	(*S*)-BINAMINE	42	132	124	208	left-handed
R3	(*R*)-BINAMINE	43	131	81	177	right-handed

[a]All NRs comprise a central achiral Au NR, on which a chiral Au shell was grown using surfactant micelle templating, using either (*R*)-BINAMINE/CTAC or (*S*)-BINAMINE/CTAC mixtures.

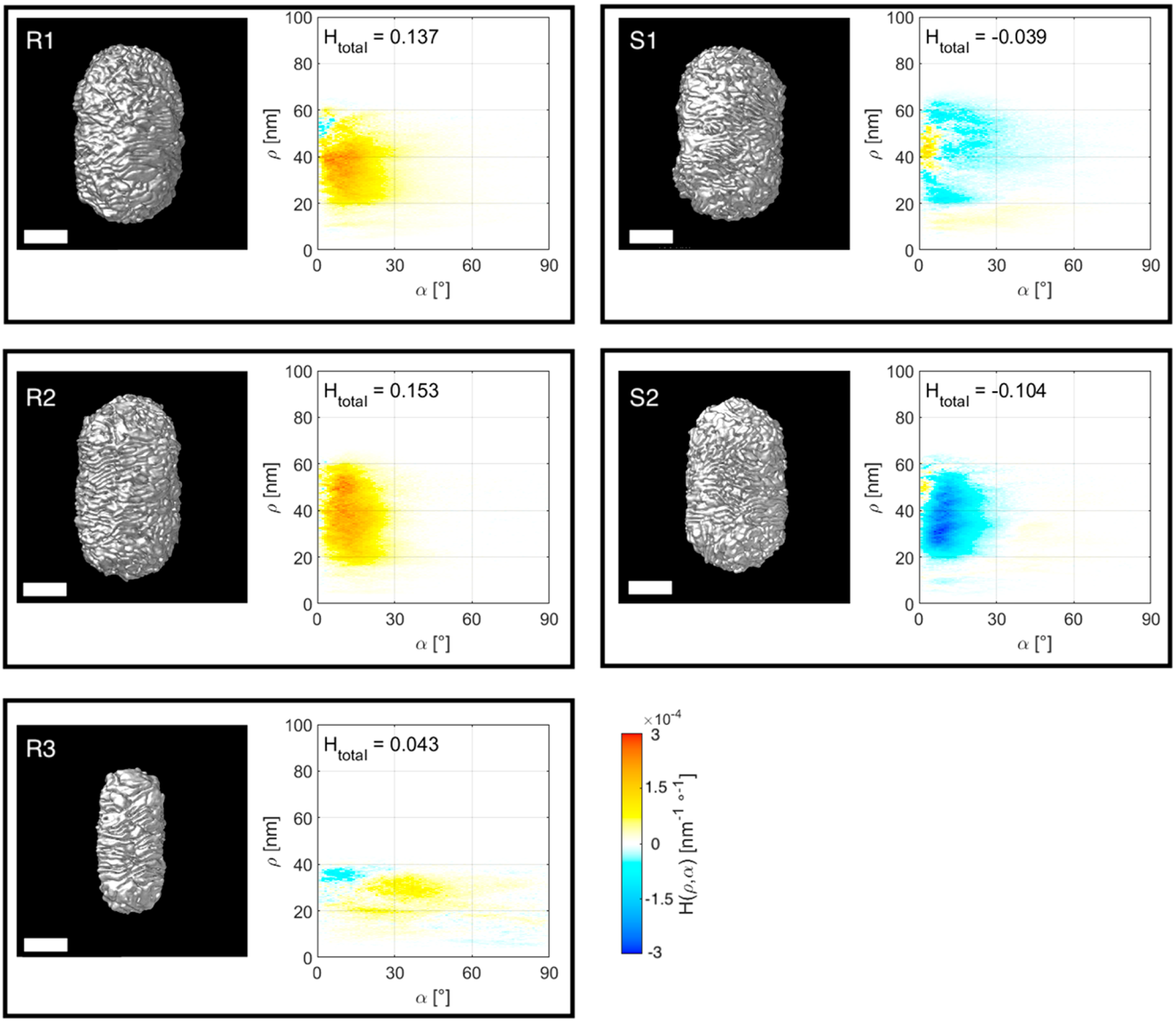

Figure 3. Isosurface visualizations of the 3D ET reconstructions for five chiral Au NRs, described in Table 1 (left image in each panel), along with a plot of the corresponding helicity function $H(\rho,\alpha)$ (right image in each panel). The total helicity H_{total} is also indicated for each Au NR. All scale bars are 50 nm.

EXPERIMENTAL RESULTS

Au NRs. To illustrate the use of our method, we investigated 3D reconstructions of Au NRs synthesized by micelle-templated seeded growth on achiral Au NRs.[10] Since these particles were analyzed in earlier work, we use them as a proof of principle for our methodology. A chiral shell was grown on the Au NR seeds using cetyltrimethylammonium chloride (CTAC) as a surfactant, combined with either (*R*)-BINAMINE for right-handed chiral NRs or (*S*)-BINAMINE for left-handed chiral NRs. BINAMINE (1,1′-binaphthyl-2,2′-diamine) is a derivative of BINOL (1,1′-bi(2-naphthol)) and acts as a chiral cosurfactant to create helical micelles.[38] Using this approach, chiral Au NRs of different dimensions can be prepared, which may slowly reshape over time because of a limited thermodynamic stability. Therefore, the thiolated amino acid cysteine was used as a stabilizing agent to prevent

https://doi.org/10.1021/acsmaterialslett.2c00055
ACS Materials Lett. 2022, 4, 642−649

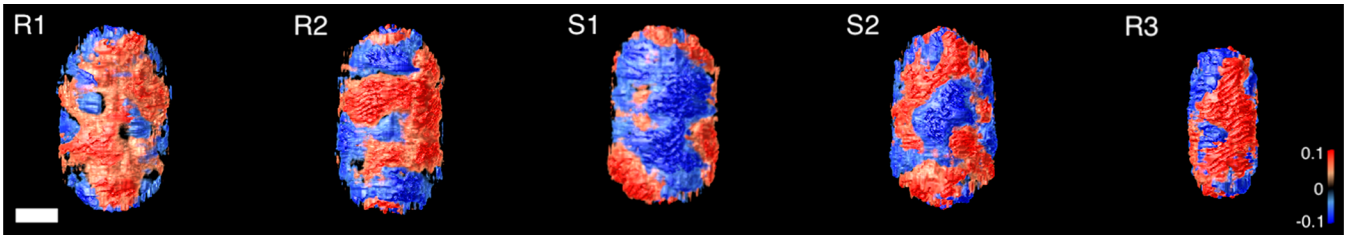

Figure 4. 3D color-coded volume renderings of the helicity maps for the particles described in Table 1. Red indicates right-handed helical features; blue indicates left-handedness. The scale bar (valid for all images) represents 50 nm.

reshaping. The reader is referred to the SI and ref 10 for complete details on synthesis and ET procedures. Here, we selected five different NRs, as listed in Table 1. Two of the selected particles (R1 and R2) were obtained from the same sample, prepared with (*R*)-BINAMINE/CTAC; two other NRs (S1 and S2) were from a sample prepared with (*S*)-BINAMINE/CTAC. The synthesis conditions for these particles were the same, except for the specific BINAMINE enantiomer. A fifth particle (R3) was prepared with (*R*)-BINAMINE/CTAC but under conditions resulting in a thinner chiral shell. More details on the synthesis and tomography reconstructions are provided in sections 3 and 4 of the SI.

3D renderings of the corresponding tomography reconstructions are shown in Figure 3 (see also orthoslices in Figure S3). Due to their thickness and the limited depth of field of the electron probe, only the front half of the particles could be reconstructed at a sufficient resolution for further quantitative analysis.[39] In Figure 3, the NRs are oriented to display their front halves, complete 3D rendering movies are provided as SI. Interestingly, our method provides the opportunity to calculate the helicity function for selected parts of the reconstruction. We therefore selected those parts of the reconstructions that showed sufficient resolution for further analysis. This approach will not introduce bias because the particles are randomly oriented on the TEM grid. Since the tips of the chiral Au NRs are dominated by randomly oriented wrinkles, they were manually removed prior to calculating the helicity functions $H(\rho,\alpha)$ and the total helicity H_{total}, presented in Figure 3. The results including the tips are shown in Figure S4, from which it is clear that the presence of random wrinkles indeed affects the results.

The H_{total} values, calculated for the particles synthesized using (*R*)-BINAMINE/CTAC (R1, R2, and R3) are all positive, as expected for right-handed helical structures, whereas those obtained using the (*S*)-enantiomer (S1 and S2) are left-handed helical (negative H_{total}). This result confirms the claim that the handedness of chiral NRs can be controlled through rational selection of the corresponding enantiomer during synthesis.[10] Moreover, the absolute value of H_{total} is similar for R1, R2, and S2, as expected because they resulted from similar synthesis conditions. On the contrary, a much lower H_{total} value was obtained for S1, which is likely due to a significant variability in the chirality of different NRs from the same sample batch, as also shown experimentally.[20,21]

In this particular system, the helicity of the particles originates from helical wrinkles in the shell. As already indicated in ref 10, the wrinkles have inclination angles ranging from $\alpha = 0°$ to $\alpha = 45°$. The plots of the helicity function $H(\rho,\alpha)$ confirm these conclusions and furthermore reveal that the larger particles (R1, R2, S1, and S2) contain mostly inclination angles between $\alpha = 0°$ and $\alpha = 25°$, with most of the helicity being concentrated around $\alpha = 10°$. On the contrary, the wrinkles for the smaller particle (R3) feature higher inclination angles, between $\alpha = 20°$ and $\alpha = 50°$. Although additional data are required to confirm this trend, the results indicate that the average angle of inclination strongly depends on the thickness of the chiral shell. To accurately investigate such a trend, one needs to acquire enough data to accurately represent the ensemble of particles in each sample.

From our analysis, it also appears that thinner chiral shells display a lower fraction with a chiral signature. This observation is also reflected in H_{total}, which is significantly lower for R3, as compared to R1 and R2. These preliminary results agree with the average optical anisotropy factors measured experimentally for right-handed chiral NRs.[10] A maximum of $g_{CD,max} = 0.12$ at a wavelength of 700 nm was recorded for the sample containing particle R3, whereas for the sample containing R1 and R2 a maximum anisotropy factor of $g_{CD,max} = 0.18$ was recorded at a wavelength of 1100 nm. As a comparison with well-defined chiral NRs, we additionally applied our methodology to two different particles discussed in ref 10. The first one has a qualitatively different helicity function $H(\rho,\alpha)$ but is still right-handed helical, whereas the second particle has poorly defined chirality (Figure S5 and section 5 in the SI), which correctly results in a much lower H_{total} value than that for the nanorods discussed in Figure 3.

Visualization of Helical Features. A purely visual inspection of the NRs indicates that they contain both left- and right-handed features, regardless of their overall handedness. It is consequently useful to identify the helicity of subregions in the particle. We therefore created 3D helicity maps to identify which features contribute most to the overall helicity. To build these maps, we calculated the helicity measure for small windows around each voxel in the particle in cylindrical coordinates and then assigned the calculated total helicity H_{total} to each voxel (Figure S6). The main drawback of this approach is that the window size must be manually selected. After comparing different window sizes, as discussed in section 6 of the SI and Figure S7, we concluded that a window size of 32 × 32 voxels is the optimal choice for this particular case.

Figure 4 shows the helicity maps for the NRs listed in Table 1. Orthoslices through these maps (Figure S8) and animated helicity maps are provided in the SI. It is observed that all chiral NRs contained both right- and left-handed features. However, arguably more right-handed features than left-handed features can be observed in globally right-handed rods and vice versa. These results are of interest to further understand the origin of the chiral features and to eventually optimize the synthesis toward NRs with enhanced optical chirality. A more elaborate analysis could include segmenting

https://doi.org/10.1021/acsmaterialslett.2c00055
ACS Materials Lett. 2022, 4, 642−649

the helicity maps and calculating the number and size of regions for each handedness.

Complex Helical Nanostructures. Although our methodology has been specifically designed for the analysis of helical NRs, the limited number of assumptions allows us to apply the approach to other helical systems, as long as a well-defined helical axis can be identified. As a representative example, we analyzed the helicity of self-assembled Au NRs around amyloid fibrils (Figure 5).[40] Such fibrils are formed by spontaneous aggregation of amyloid proteins and are known to be related to various neurodegenerative disorders. Since these fibers display a (double-)helical morphology, they could be used as a template for the helical organization of Au NRs. Under such an arrangement, the coupling of plasmonic effects from Au NRs results in optical activity that can be recorded as circular dichroism (CD). Kumar et al. proposed the use of CD signals from helically assembled Au NRs to selectively detect the presence of the fibrils.[40]

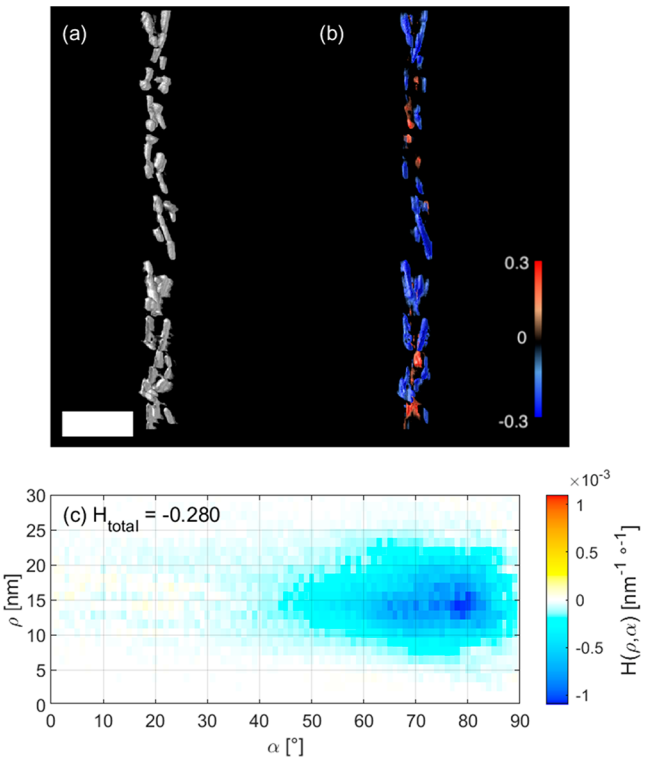

Figure 5. Quantitative analysis of the helicity of a helical arrangement of Au NRs around an amyloid fibril. An isosurface rendering of the NRs is shown in a; the helicity map is shown in b as a semitransparent 3D color-coded volume rendering, where red indicates right-handed helicity and blue indicates left-handed helicity. The window size was chosen to encompass each individual NR. The helicity function $H(\rho,\alpha)$ and total helicity H_{total} are given in c. The scale bar is 100 nm.

Characterization of one such self-assembled Au NR double-helical fibril by cryo-ET provided a 3D reconstruction that could be analyzed by our method. Figure 5 shows that the well-defined helicity of the system resulted in a value of H_{total} = −0.28, which is closer to a perfect left-handed helical object than the NRs investigated above. The helicity function $H(\rho,\alpha)$ (Figure 5c) indeed shows a strong left-handed helical signal at high inclination angles, between α = 60° and α = 85°. From the position of the peak in the helicity function, between ρ = 10 nm and ρ = 20 nm, we conclude that the nanoparticles are organized within this range of radii from the helical axis. In contrast to the findings for the helical NRs, the helicity map (Figure 5b) indicates that all regions of the cluster contribute to the left-handed helicity, with limited traces of right-handedness that originate from a few misaligned NRs.

DISCUSSION AND OUTLOOK

The method described here, for which we created a Python package (HeliQ) Python package (HeliQ),[41] is complementary to ensemble measurements and yields rich information at a single particle level. However, a few limitations must be overcome to make the approach widely applicable to any type of system. First, a helical axis must be identified manually, which currently restricts the use of our method to NRs, nanowires, and similar elongated structures. This became apparent when analyzing the NRs in Figure 3, where the seemingly random orientations of the wrinkles at the tips of the NRs were found to introduce artifacts in the results. Namely, one could hypothesize that the wrinkles at the tips are also helical, but with a different helical axis. An alternative possibility might involve using a 3D gradient to (locally) detect the helical axis. Another limitation lies in the current normalization of the directionality. If only a few features are present in a cylindrical section (i.e., if that section has a nearly uniform intensity), then the normalization factor will be small, artificially increasing the intensity in the helicity function $H(\rho,\alpha)$. An example of this behavior is shown in the achiral NR in Figure S5. As discussed in the SI, this mainly becomes a problem for nonhelical, axially symmetric particles. A different normalization factor could be the solution for this problem. Finally, it should also be noted that our methodology is designed for quantifying helicity rather than chirality. Chirality in general is a much more abstract characteristic, which can be divided in two groups: handed and nonhanded chirality.[42] Handed chirality refers to all objects that can be assigned a handedness unambiguously, and helicity is a type of handed chirality. This means that also chiral particles can be classified as nonhelical. Nonetheless, the total helicity H_{total} accurately identifies the second particle in Figure S5 as achiral. Taking the current limitations into account, future modifications of our methodology will likely make it generally applicable to any shape.

CONCLUSIONS

We introduced a method for the quantitative analysis of morphological helicity, which has been exemplarily applied to electron tomography reconstructions of chiral Au nanorods. The approach is based on the geometrical properties of a helix and results in a two-dimensional helicity function $H(\rho,\alpha)$, which can be interpreted as the decomposition of a given shape into a combination of helices. The helicity function provides spatially resolved information about the presence of helical features, as well as their inclination angles. A numerical parameter, the total helicity H_{total}, obtained as the integral over the full helicity function, gives an overall indication of the helical degree for a given particle. Analyses of ET reconstructions of chiral Au NRs agree with previous observations, while additionally providing more quantitative parameters, such as the angle of inclination of helical features. This information may eventually help understanding the effect of various synthesis parameters. The more general applicability

https://doi.org/10.1021/acsmaterialslett.2c00055
ACS Materials Lett. 2022, 4, 642−649

of the approach was demonstrated through the analysis of a helical nanostructure composed of Au NRs clustered around a fibrillar protein template; a high degree of helicity throughout the entire superhelical nanostructure was confirmed, in agreement with previous experimental measurements. Further generalization of this approach should be possible by automation of the selection of parameters such as window size and determination of the helical axis.

■ ASSOCIATED CONTENT

Supporting Information

Movies (MPG and MP4) visualizing the morphology and helicity map of particle X in 3D, with X: R1, R1, R2, R2, S1, S1, S2, S2, R3, R3, P1, P1, P2, P2; Movies 15 and 16 visualize the helical clusters; Movie 17 visualizes the electron tomography tilt series of particle R2. The Supporting Information is available free of charge at https://pubs.acs.org/doi/10.1021/acsmaterialslett.2c00055.

Additional images, synthesis, and computational details (PDF)
Movie (MPG)
Movie (MPG)
Movie (MPG)
Movie (MPG)
Movie (MPG)
Movie (MPG)
Movie (MPG)
Movie (MPG)
Movie (MPG)
Movie (MPG)
Movie (MPG)
Movie (MPG)
Movie (MPG)
Movie (MPG)
Movie (MPG)
Movie (MPG)
Movie (MP4)

■ AUTHOR INFORMATION

Corresponding Authors

Sara Bals − *EMAT and NANOlab Center of Excellence, University of Antwerp, 2020 Antwerp, Belgium;* orcid.org/0000-0002-4249-8017; Email: Sara.Bals@uantwerpen.be

Wiebke Albrecht − *EMAT and NANOlab Center of Excellence, University of Antwerp, 2020 Antwerp, Belgium; Center for Nanophotonics, AMOLF, 1098 XG Amsterdam, The Netherlands*; Email: W.Albrecht@amolf.nl

Authors

Wouter Heyvaert − *EMAT and NANOlab Center of Excellence, University of Antwerp, 2020 Antwerp, Belgium;* orcid.org/0000-0002-1152-3240

Adrián Pedrazo-Tardajos − *EMAT and NANOlab Center of Excellence, University of Antwerp, 2020 Antwerp, Belgium*

Ajinkya Kadu − *EMAT and NANOlab Center of Excellence, University of Antwerp, 2020 Antwerp, Belgium*

Nathalie Claes − *EMAT and NANOlab Center of Excellence, University of Antwerp, 2020 Antwerp, Belgium*

Guillermo González-Rubio − *CIC biomaGUNE, Basque Research and Technology Alliance (BRTA), 20014 Donostia-San Sebastián, Spain; Physical Chemistry Department, University of Konstanz, 78457 Konstanz, Germany*

Luis M. Liz-Marzán − *CIC biomaGUNE, Basque Research and Technology Alliance (BRTA), 20014 Donostia-San Sebastián, Spain; Centro de Investigación Biomédica en Red de Bioingeniería, Biomateriales y Nanomedicina (CIBER-BBN), 20014 Donostia-San Sebastián, Spain; Ikerbasque, Basque Foundation for Science, 48009 Bilbao, Spain;* orcid.org/0000-0002-6647-1353

Complete contact information is available at: https://pubs.acs.org/10.1021/acsmaterialslett.2c00055

Author Contributions

The manuscript was written through contributions of all authors. All authors have given approval to the final version of the manuscript.

Notes

The authors declare no competing financial interest.

■ ACKNOWLEDGMENTS

S.B. and A.P.-T. gratefully acknowledge funding by the European Research Council (ERC Consolidator Grant #815128-REALNANO) the European Union's Horizon 2020 research and innovation program under grant agreement #823717—ESTEEM3. L.M.L.-M. acknowledges funding from MCIN/ AEI /10.13039/501100011033, grant # PID2020-117779RB-I00 and the Maria de Maeztu Units of Excellence Program from the Spanish State Research Agency (Grant No. MDM-2017-0720). G.G.-R. thanks the Spanish Spanish Ministerio de Ciencia e Innovación for an FPI (BES-2014-068972) fellowship.

■ REFERENCES

(1) Zheng, G.; He, J.; Kumar, V.; Wang, S.; Pastoriza-Santos, I.; Pérez-Juste, J.; Liz-Marzán, L. M.; Wong, K.-Y. *Chem. Soc. Rev.* **2021**, *50*, 3738−3754.
(2) Lv, H.; Mou, Z.; Zhou, C.; Wang, S.; He, X.; Han, Z.; Teng, S. *Nanotechnology.* **2021**, *32*, 315203.
(3) Shukla, N.; Bartel, M. A.; Gellman, A. J. *J. Am. Chem. Soc.* **2010**, *132*, 8575−8580.
(4) Gautier, C.; Bürgi, T. *ChemPhysChem.* **2009**, *10*, 483−492.
(5) Roy, S.; Pericàs, M. A. *Org. Biomol. Chem.* **2009**, *7*, 2669−2677.
(6) Link, S.; Hartland, G. V. *J. Phys. Chem. C* **2021**, *125*, 10175−10178.
(7) Bürgi, T. *CHIMIA.* **2011**, *65*, 157−167.
(8) Zhao, S.; Shao, L.; Wang, J.; Lin, H.-Q.; Zhang, W. *Photon. Res.* **2021**, *9*, 484−493.
(9) Lee, H.-E.; Ahn, H.-Y.; Mun, J.; Lee, Y. Y.; Kim, M.; Cho, N. H.; Chang, K.; Kim, W. S.; Rho, J.; Nam, K. T. *Nature.* **2018**, *556*, 360−365.
(10) González-Rubio, G.; Mosquera, J.; Kumar, V.; Pedrazo-Tardajos, A.; Llombart, P.; Solís, D. M.; Lobato, I.; Noya, E. G.; Guerrero-Martínez, A.; Taboada, J. M.; Obelleiro, F.; Macdowell, L. G.; Bals, S.; Liz-Marzán, L. M. *Science.* **2020**, *368*, 1472−1477.
(11) Sobczak, K.; Turczyniak-Surdacka, S.; Lewandowski, W.; Baginski, M.; Tupikowska, M.; González-Rubio, G.; Wójcik, M.; Carlsson, A.; Donten, M. *Microsc. Microanal.* **2021**, 1−5.
(12) Esposito, M.; Tasco, V.; Todisco, F.; Cuscunà, M.; Benedetti, A.; Sanvitto, D.; Passaseo, A. *Nat. Commun.* **2015**, *6*, 6484.
(13) Furusawa, G.; Kan, T. *Micromachines.* **2020**, *11*, 641.
(14) Chen, J.; Gao, X.; Zheng, Q.; Liu, J.; Meng, D.; Li, H.; Cai, R.; Fan, H.; Ji, Y.; Wu, X. *ACS Nano* **2021**, *15*, 15114−15122.
(15) Zhang, L.; Wang, T.; Shen, Z.; Liu, M. *Adv. Mater.* **2016**, *28*, 1044−1059.

(16) Frank, B.; Yin, X.; Schäferling, M.; Zhao, J.; Hein, S. M.; Braun, P. V.; Giessen, H. *ACS Nano* **2013**, *7*, 6321−6329.
(17) Londoño-Calderon, A.; Williams, D. J.; Schneider, M. M.; Savitzky, B. H.; Ophus, C.; Ma, S.; Zhu, H.; Pettes, M. T. *Nanoscale.* **2021**, *13*, 9606−9614.
(18) Solomon, E. I.; Lever, A. B. P. *Inorganic Electronic Structure and Spectroscopy*; Wiley, 2006; Vol. *1*.
(19) Spaeth, P.; Adhikari, S.; Le, L.; Jollans, T.; Pud, S.; Albrecht, W.; Bauer, T.; Caldarola, M.; Kuipers, L.; Orrit, M. *Nano Lett.* **2019**, *19*, 8934−8940.
(20) Karst, J.; Cho, N. H.; Kim, H.; Lee, H.-E.; Nam, K. T.; Giessen, H.; Hentschel, M. *ACS Nano* **2019**, *13*, 8659−8668.
(21) Smith, K. W.; Zhao, H.; Zhang, H.; Sanchez-Iglesias, A.; Grzelczak, M.; Wang, Y.; Chang, W.-S.; Nordlander, P.; Liz-Marzan, L. M.; Link, S. *ACS Nano* **2016**, *10*, 6180−6188.
(22) Gutsche, P.; Garcia-Santiago, X.; Schneider, P.-I.; McPeak, K. M.; Nieto-Vesperinas, M.; Burger, S. *Symmetry.* **2020**, *12*, 158.
(23) Canfield, B. K.; Kujala, S.; Laiho, K.; Jefimovs, K.; Turunen, J.; Kauranen, M. *Opt. Express.* **2006**, *14*, 950−955.
(24) Maoz, B. M.; Chaikin, Y.; Tesler, A. B.; Bar Elli, O.; Fan, Z.; Govorov, A. O.; Markovich, G. *Nano Lett.* **2013**, *13*, 1203−1209.
(25) Nemati, A.; Shadpour, S.; Querciagrossa, L.; Li, L.; Mori, T.; Gao, M.; Zannoni, C.; Hegmann, T. *Nat. Commun.* **2018**, *9*, 3908.
(26) Cho, N. H.; Byun, G. H.; Lim, Y.-C.; Im, S. W.; Kim, H.; Lee, H.-E.; Ahn, H.-Y.; Nam, K. T. *ACS Nano* **2020**, *14*, 3595−3602.
(27) Lee, H.-E.; Kim, R. M.; Ahn, H.-Y.; Lee, Y. Y.; Byun, G. H.; Im, S. W.; Mun, J.; Rho, J.; Nam, K. T. *Nat. Commun.* **2020**, *11*, 263.
(28) Weyland, M.; Midgley, P. A. *Mater. Today.* **2004**, *7*, 32−40.
(29) Ben-Moshe, A.; Wolf, S. G.; Sadan, M. B.; Houben, L.; Fan, Z.; Govorov, A. O.; Markovich, G. *Nat. Commun.* **2014**, *5*, 4302.
(30) Yewande, E. O.; Neal, M. P.; Low, R. *Mol. Phys.* **2009**, *107*, 281−291.
(31) Podolak, J.; Shilane, P.; Golovinskiy, A.; Rusinkiewicz, S.; Funkhouser, T. *ACM Transitions on Graphics.* **2006**, *25*, 549−559.
(32) Kazhdan, M.; Chazelle, B.; Dobkin, D.; Funkhouser, T.; Rusinkiewicz, S. *Algorithmica.* **2004**, *38*, 201−225.
(33) Kamberaj, H.; Osipov, M. A.; Low, R. J.; Neal, M. P. *Mol. Phys.* **2004**, *102*, 431−446.
(34) Osipov, M. A.; Pickup, B. T.; Dunmur, D. A. *Mol. Phys.* **1995**, *84*, 1193−1206.
(35) Bai, L.; Kämäräinen, T.; Xiang, W.; Majoinen, J.; Seitsonen, J.; Grande, R.; Huan, S.; Liu, L.; Fan, Y.; Rojas, O. J. *ACS Nano* **2020**, *14*, 6921−6930.
(36) Kelvin, W. T. *The Molecular Tactics of a Crystal*; University of California Libraries, 1894.
(37) Tinevez, J.-Y.; Rueden, C. Directionality. https://imagej.net/plugins/directionality (Accessed December, 2021).
(38) Ito, T. H.; Salles, A. G.; Priebe, J. P.; Miranda, P. C. M. L.; Morgon, N. H.; Danino, D.; Mancini, G.; Sabadini, E. *Langmuir.* **2016**, *32*, 8461−8466.
(39) Altantzis, T.; Wang, D.; Kadu, A.; van Blaaderen, A.; Bals, S. *J. Phys. Chem. C* **2021**, *125*, 26240−26246.
(40) Kumar, J.; Eraña, H.; López-Martínez, E.; Claes, N.; Martín, V. F.; Solís, D. M.; Bals, S.; Cortajarena, A. L.; Castilla, J.; Liz-Marzán, L. M. *PNAS.* **2018**, *115*, 3225−3230.
(41) Heyvaert, W.; Bals, S.; Albrecht, W. *HeliQ. Zenodo*; Zenodo, 2022; DOI: 10.5281/zenodo.5873546.
(42) King, B. *Ann. N.Y. Acad. Sci.* **2003**, *988*, 158−170.

https://doi.org/10.1021/acsmaterialslett.2c00055
ACS Materials Lett. 2022, 4, 642−649